Ceramics



Phase development of silicon oxycarbide nanocomposites during flash pyrolysis

Lixia Wang^{1,2} and Kathy Lu^{2,*} (b)

Received: 1 October 2018 Accepted: 1 January 2019 Published online: 7 January 2019

© Springer Science+Business Media, LLC, part of Springer Nature 2019

ABSTRACT

This work is focused on phase development of silicon oxycarbide (SiOC) nanocomposites during flash pyrolysis. Three important variables evaluated are applied electric field, current limit, and pyrolysis temperature. They significantly facilitate the microstructure evolution of SiOC and cause the formation of more ordered carbon and SiC phases at > 640 °C lower temperature than the typical pyrolysis process. With the increase in the applied electric field, pyrolysis temperature, and current density, the mass loss is higher, the SiC formation and carbon precipitation are more extensive, and the carbon phase is more ordered. The resulting SiOC samples are stable up to 742 °C in air. The fundamental cause is due to the drastically accelerated nucleation rate for both the C and SiC phases from the applied electrical field, through the mechanisms of Joule heating and electromigration. This work provides an accelerated route to synthesize high-temperature SiOC nanocomposites.

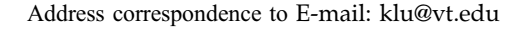
Introduction

Silicon oxycarbide ceramics (SiOCs) are novel polymer-derived ceramics that show high flexibility in tailoring microstructures and phases with a composition of SiC_xO_{4-x} ($1 \le x \le 3$) [1]. They exhibit excellent mechanical strength [2–5], thermal stability [6], and creep resistance [7]. They are also a desirable reaction bonding phase for SiC particles (1000–1200 °C) [8, 9].

Pyrolysis is a versatile technique to prepare SiOC nanocomposites via phase evolution from cross-linked precursors [10, 11]. The SiOC matrix evolves

into a system containing nano-sized amorphous SiO_2 clusters and a disordered carbon phase at ~ 1100 °C pyrolysis temperature [12–14]; and SiC nanocrystals form at > 1300 °C pyrolysis temperatures [15].

From a different perspective, flash sintering has raised great interest since 2010 [16]. This process is capable of inducing a sudden onset of densification through Joule heating [17], which can heat the sample several hundred degrees Celsius higher than the furnace temperature [16]. Under the temperature increase, the electrical conductivity of the sample increases drastically and the flash process stops. Flash sintering can be divided into three main stages. The first is the incubation period, during which the





¹Key Laboratory of Applied Chemistry, College of Chemistry and Chemical Engineering, Bohai University, Jinzhou 121013, China

²Department of Materials Science and Engineering, Virginia Polytechnic Institute and State University, Blacksburg, VA 24061, USA

system works in a voltage control mode, and the power dissipation and electrical current slowly increase. The second stage is a "far from the equilibrium stage," where the material undergoes the flash event. During this period, electrical resistivity consistently decreases and a heating rate on the order of 104 K/min is achieved; power density reaches a peak and the system is typically switched from voltage control to current control [18]. During the third stage, also known as the steady stage, the system reaches a new equilibrium condition (i.e., electrical parameters and power dissipation are stabilized). During this period, microstructure evolution occurs.

Different studies have employed electrical field assisted techniques to obtain dense SiOC materials [3, 19, 20]. However, the SiOC materials in these studies are pyrolyzed before sintering and preparation of polymer-derived ceramics such as SiOCs by electrical field assisted pyrolysis has not yet been well studied. Since the SiOC systems are insulating before a large amount of ordered carbon forms, the Joule heating can be substantial and thus induce a sudden temperature increase. When the carbon phase undergoes ordering, the flash process may induce even further changes within the SiOC matrix [21].

This work is focused on the flash pyrolysis of polysiloxanes into SiOC materials. The derived SiOC ceramics have been characterized using X-ray diffraction (XRD), transmission electron microscopy (TEM), thermogravimetric analysis (TGA), and Raman spectroscopy. The thermoelectric changes, SiOC phase evolution, microstructures, and oxidation resistance were evaluated. The driving forces for the nucleation and phase separation with and without an external electrical field were studied. Based on this, we explained the much lower phase formation temperatures for the C and SiC species.

Materials and methods

Material preparation

Commercial polysiloxanes (vinyl-terminated polyphenylmethylsiloxane (PMPS) and polyhydromethylsiloxane (PHMS)) were used as the base precursors and 2.1–2.4% platinum–divinyltetramethyldisiloxane complex in xylene (Pt catalyst) was used as the catalyst. All the above chemicals were from Gelest Inc., Morrisville, PA.

Samples were obtained by catalytic cross-linking of PMPS and PHMS. The PHMS/PMPS weight ratio was 15/85. First, a solution with the polymer precursors PMPS and PHMS was sonicated for 10 min. They were then homogenized in a high energy mill (SPEX 8000 M Mixer/Mill, SPEX Sample Prep, Metuchen, NJ) for 10 min. Next, the Pt catalyst (5 ppm relative to PHMS) was added. After that, the mixtures were homogenized again in the Spex mill for 5 min. The solution was finally poured into aluminum foil molds, which were put into a vacuum chamber and vacuumed for 10 min at 1500 m Torr (and room temperature) to remove any bubbles in the solutions. The filled molds were then placed in an oven to crosslink at 50 °C for 12 h and then at 120 °C for 6 h.

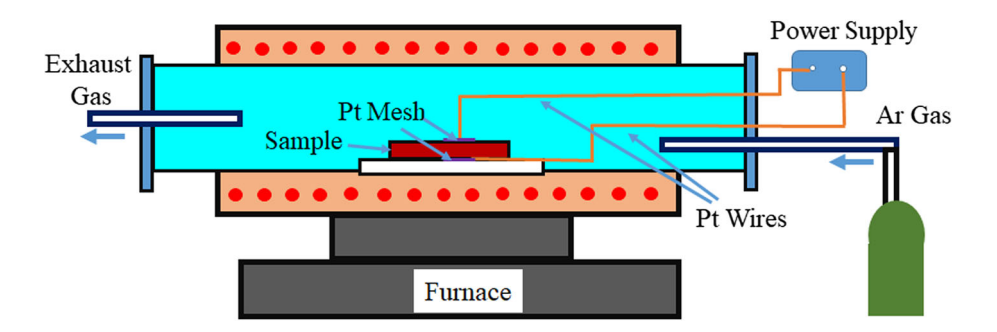
Flash pyrolysis

The cross-linked green samples were cut and then polished into cylindrical shapes (~ 12 mm in diameter and 2–3 mm in thickness) for calculation convenience. A silver–palladium paste (conductor type 9627, ESL ElectroScience, King of Prussia, PA) was applied to the faces of each sample in order to achieve good electrical contact (minimizing contact resistance) and serve as the electrodes for the flash pyrolysis. The sample was connected through Pt wires to an external power supply and then placed into a zirconia crucible.

The sample was pyrolyzed in a tube furnace (1730-20 Horizontal Tube Furnace, CM Furnaces Inc., Bloomfield, NJ). An argon atmosphere with a flow rate of about 70 std cm³/s was used. The flash pyrolysis setup is shown in Fig. 1. The furnace heating rate was 5 °C/min from room temperature to 300 °C. After that it was 2 °C/min to the desired temperature of 740–780 °C. At the peak temperature, an electric field (0, 20, 30, 40, or 50 V/mm) was applied. We used two DC power sources (Bertan 210-01R Spellman, Hauppauge, NY and FB200 Fisher Scientific, Oreland, PA) to apply a specific voltage to the specimens. When a flash occurred, the power supply automatically switched to the current control mode. Experiments were carried out with the current change from 0.5 to 2 A, and the power supply was stopped shortly after the flash occurred. Additional control samples were pyrolyzed to 1400 °C without any applied electric field following the same heating procedure. This traditional pyrolysis temperature



Figure 1 Flash pyrolysis setup used in this study.



was chosen in order to clearly demonstrate the effectiveness of flash pyrolysis based on the sample internal temperature calculation from Eq. (2) and the data in Table 1 (to be presented later).

Parameters of electrical field assisted pyrolysis

The samples were labeled as $T_{\rm F}$ -E-I, where $T_{\rm F}$ is the pyrolysis furnace temperature (740 °C, 760 °C, 770 °C, and 780 °C), E is the electric field applied to the sample (0, 20, 30, 40, and 50 V/mm), and I is the current limit set on the power supply (0.5, 1.0, 1.5, and 2 A).

The power density $P_{\rm W}$ (mW/mm³) has been calculated according to the relationship [22]:

$$P_{\mathbf{W}} = E_i \tag{1}$$

where j is current density, A/mm².

During the flash pyrolysis, the insulating nature of the polymer precursors and decomposed radicals created a state that a large amount of Joule heating was generated, which, as expected, caused drastic sample temperature increase. Because of such local heating, the actual temperature inside the sample during the flash process was much greater than the

Table 1 Internal temperatures of the flash-pyrolyzed samples according to Eq. (2)

Samples	$P_{\rm w}~({\rm mW/mm}^3)$	T (°C)
760-40-2.0	300	1306.9
770-40-2.0	321	1345.2
780-40-2.0	249	1278.3
770-30-2.0	247	1261.2
770-50-2.0	273	1292.0
770-40-0.5	151	1127.5
770-40-1.0	195	1193.3
770-40-1.5	240	1252.5

indicated furnace temperature. The sample internal temperature (*T*) during the flash can be estimated based on blackbody radiation using the following equation [17, 23, 24]:

$$T = T_{\rm F}\alpha \left[1 + \frac{1000P_{\rm W}}{\sigma_{\rm SF}T_{\rm F}^4} \left(\frac{V}{A} \right) \right]^{\frac{1}{4}} \tag{2}$$

where $T_{\rm F}$ is the furnace temperature at the onset of the flash in Kelvin, $\sigma_{\rm SF}$ is the Stefan–Boltzmann constant with a value of 5.67 × 10⁻⁸ Wm⁻² K⁻⁴, α is a correction factor to account for emissivity less than that expected for a perfect blackbody (approximately 1), V is the volume of the specimen in m³, and A is the total surface area of the specimen in m².

Characterization

The phase compositions of the pyrolyzed samples were analyzed in an X'Pert PRO diffractometer (PANalytical B.V., EA Almelo, the Netherlands) with Cu K α radiation. The size of the SiC nanocrystallites can be calculated using the Scherrer's equation based on the full width at half maximum (FWHM) of the (111) peak for β -SiC [25]:

$$d = \frac{k\lambda}{B\cos\theta} \tag{3}$$

where d is the mean crystallite size, k is a constant usually equal to 0.9, λ is the wavelength of Cu K_{\alpha} radiation (λ = 1.5405 Å), B is the full width at half maximum intensity of the peak (FWHM) in radian, and θ is Bragg's diffraction angle. The microstructures of the pyrolyzed ceramics were analyzed using transmission electron microscopy (JEOL 2100, JEOL USA, Peabody, MA); the samples were prepared by grinding into a powder and then dispersing in absolute ethanol before being placed on TEM grids. Raman spectra were obtained using a Horiba spectrometer (JY Horiba HR 800, Edison, NJ) at 514 nm excitation wavelength, which was produced by an Ar



laser between the spectral range of 500–3500 cm⁻¹. The thermal stability of the SiOC samples after the flash pyrolysis was investigated using a Q50 TGA (TA Instruments, New Castle, DE) up to 900 °C at a heating rate of 5 °C/min and an air flow of 40 ml/min.

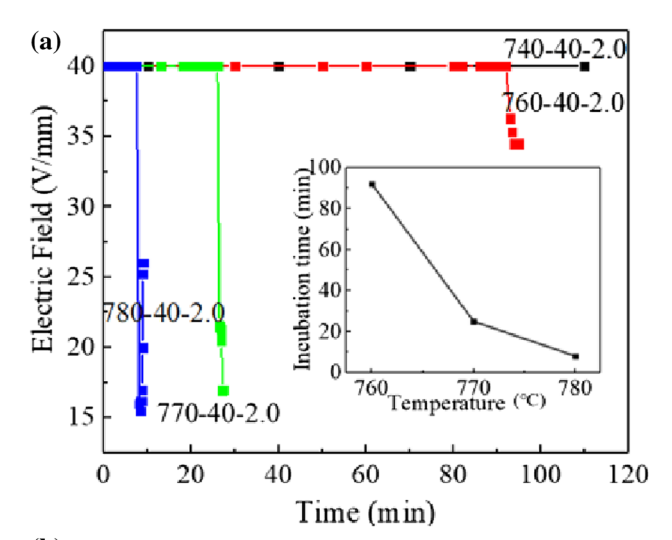
Results and discussion

Effect of flash pyrolysis temperature

For the samples flash-pyrolyzed at 740 °C, 760 °C, 770 °C, and 780 °C, Fig. 2 shows the electric field change with time at different pyrolysis temperatures (a) and the XRD patterns of the corresponding samples (b). The initial electrical field is 40 V/mm and the current limit is 2.0 A. The correlations between the flash time and current density as well as between the flash time and power density are shown in Figs. S1 and S2 in supplement. The power supply was stopped 20 s after the onset of the flash for all the samples. The starting point of the x-axis represents the time point when the DC electric field is applied.

During the flash pyrolysis, no current can be detected in the 740-40-2.0 sample even after applying the electric field of 40 V/mm for 1 h at 740 °C (Fig. S1). The XRD analysis shows that there is no phase separation in this sample (Fig. 2b). When the temperature is 760 °C and above (Fig. S2), the power density increases rapidly for the SiOC samples. This is because under the simultaneous influence from the applied electric field and the Joule heating, the specimen becomes electrically conductive, causing the electrical conductivity increase. The sudden increases in the power density and the current density and the decrease in the electric field are shown in Fig. 2a and Figs. S1–S2.

For the samples pyrolyzed at different temperatures, Fig. 2b shows their XRD patterns. Except for the 740 °C-40-2.0 sample, all the other XRD patterns show an amorphous halo at $\sim 22^{\circ}$ and diffraction peaks at 35.7°, 41.5°, 60.1°, and 72.0°. The former is from the amorphous SiO₂ and the latter corresponds to the β -SiC (111), (200), (220), and (311) crystallographic planes (JCPDS Card No. 01-073-1665) [26]. There are no clear carbon peaks because the carbon phase is mostly amorphous. Even with ordering, the carbon phase has only 2–4 graphene layers (shown in Fig. 5, TEM images), which is not enough to generate



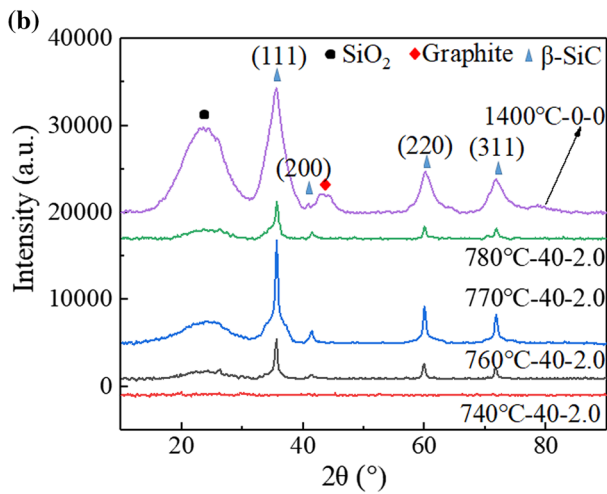


Figure 2 a Correlations between the flash time and the applied electric field, and b XRD patterns at different temperatures.

discernable XRD peaks. Figure 2b indicates that the phase separation in the samples starts from 760 °C. Compared to the traditional pyrolysis at 1400 °C, this phase separation temperature is > 640 °C lower, which means that the flash pyrolysis has tremendous beneficial effects on lowering the pyrolysis temperature without compromising the phase development.

As well known, phase separation of the SiOC matrix leads to the formation of SiO_2 , C, and SiC phases during pyrolysis at ~ 1200 °C. SiC crystallization can further occur by the carbothermal reduction in the SiO_2 phase at > 1300 °C pyrolysis temperature [6, 27]:

$$SiOC \rightarrow SiO_2 + SiC + C$$
 (4)

$$SiO_2 + C \rightarrow SiC$$
 (5)



In this study, the drastically accelerated phase separation is partly because the samples have more carbon from the precursors; it is easier to create the flash event in the sample and thus generate SiC. In conjunction with the TEM and Raman results to be discussed later, it can be seen that the carbon-rich nature in the samples is conductive for forming a large amount of SiC. The strong SiC peaks in Fig. 2b mean that SiC has better crystallinity, even though the other phases are mostly amorphous.

Based on Eq. (2), the internal temperature for each sample during the flash can be estimated. It is 1306.9 °C for the 760-40-2.0 sample ($P_{\rm w} \sim 300 \; {\rm mW}/$ mm³), 1345.2 °C for the 770-40-2.0 sample ($P_{\rm w} \sim 321$ mW/mm³), and 1278.3 °C for the 780-40-2.0 sample $(P_{\rm w} \sim 249 \text{ mW/mm}^3)$ (Table 1). With the understanding that actual systems always have lower emissivities than a perfect blackbody, α will be higher. Subsequently, the actual sample temperature will be higher than the above calculated values [17]. Because these internal temperatures are all lower than 1400 °C, the 1400 °C sample pyrolyzed without any electric field has been used as a reference in this work. Further, the XRD pattern of the 770-40-2.0 sample is very similar to that of the 1400-0-0.0 sample (Fig. 2b), confirming that the 770-40-2.0 sample has been exposed to Joule heating close to or higher than the temperature predicted by Eq. (2). Clearly, increasing the applied electric field or the current density can facilitate the SiOC phase separation, leading to the SiC phase formation at a pyrolysis temperature of 770 °C or lower. Figure 2b also shows that the SiC XRD peaks are sharper (less broadened) and the SiC phase formation is more accelerated under the flash pyrolysis.

For the 760-40-2.0, 770-40-2.0, and 780-40-2.0 samples, the incubation time t for the flash event is 90 min, 25 min, and 8 min, respectively. As the temperature increases, the incubation time becomes shorter (Fig. 2a insert) and the power density is lower, which lead to a lower internal temperature for the 780-40-2.0 sample. Thus, the corresponding SiC XRD diffraction peaks are weaker than those of the 770-40-2.0 samples. On the other hand, the 760-40-2.0 sample has a modest internal temperature and the SiC XRD diffraction peaks are weaker because the Si and C diffusion rates are slower. The 770-40-2.0 sample has the highest internal temperature, so the SiC XRD diffraction peaks are the sharpest.

The SiC crystallite size for the conventionally pyrolyzed sample at 1400 °C without an electric field, the 760 °C-40-2 sample, the 770 °C-40-2.0 sample, and the 780 °C-40-2 sample are 2.7 nm, 7.6 nm, 7.8 nm, and 7.0 nm, respectively (Fig. 4c). This is consistent with the sharp SiC diffraction peaks in Fig. 2b for the pyrolyzed samples and means that the SiC crystallization is more developed under the flash pyrolysis.

Effect of flash electric field

Figure 3 shows the flash parameters and XRD patterns at different electric field (0, 20, 30, 40, and 50 V/ mm) and 770 °C pyrolysis temperature. All the samples have the same current limit of 2.0 A when the flash occurs. The 770-20-2.0 sample has no current generation after 1 h at 770 °C and 20 V/mm electric field (Fig. S3). No phase separation occurs in this sample due to the low phase evolution driving force. At > 20 V/mm electrical field, for the 770-30-2.0, 770-40-2.0, and 770-50-2.0 samples, the drastic power density and current density increases as well as the electric field decrease over time are given in Fig. 3a and Figs. S3-S4. The incubation time t for the flash event is 55 min, 25 min, and 21 min, respectively (Fig. 3a insert). This suggests that, as the electrical field increases, the incubation time becomes drastically shorter.

For the samples pyrolyzed under different electric field, Fig. 3b shows the XRD patterns. Again, except for the 770 °C-0-0.0 sample, all the other XRD patterns have an amorphous halo at $\sim 22^{\circ}$ for SiO₂. The diffraction peaks at 35.7°, 41.5°, 60.1°, and 72.0° are from the β -SiC (111), (200), (220), and (311) crystallographic planes (JCPDS Card No. 01-073-1665) [26]. This is because the electric field significantly accelerates the SiC phase nucleation rate; more importantly, it induces carbon ordering through electromigration. As a result, the electric field leads to the early onset of the phase separation and SiC formation.

The internal temperatures of all the samples are between 1127.5 and 1345.2 °C according to Eq. (2). Interestingly, the 770-40-2.0 sample has the highest internal temperature of 1345.2 °C at 40 V/mm electrical field. The internal temperature at 50 V/mm electrical field for the 770-50-2.0 sample is lower due to the smaller current generated in the sample, at 1292.0 °C. For the 30 V/mm electrical field (770-30-2.0), the incubation time for the flash event more than



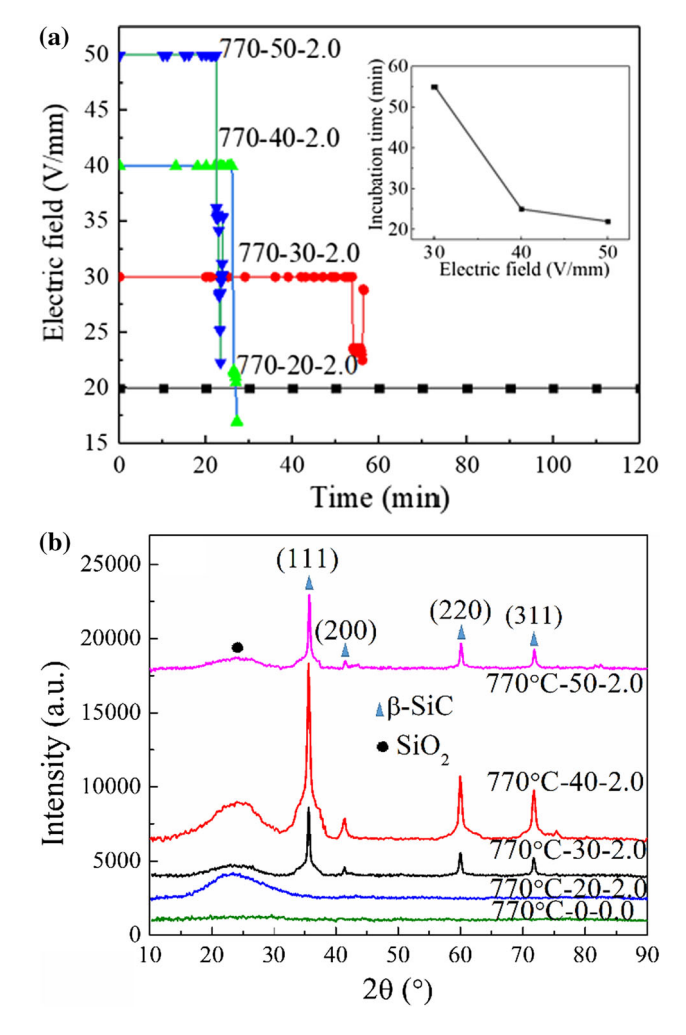
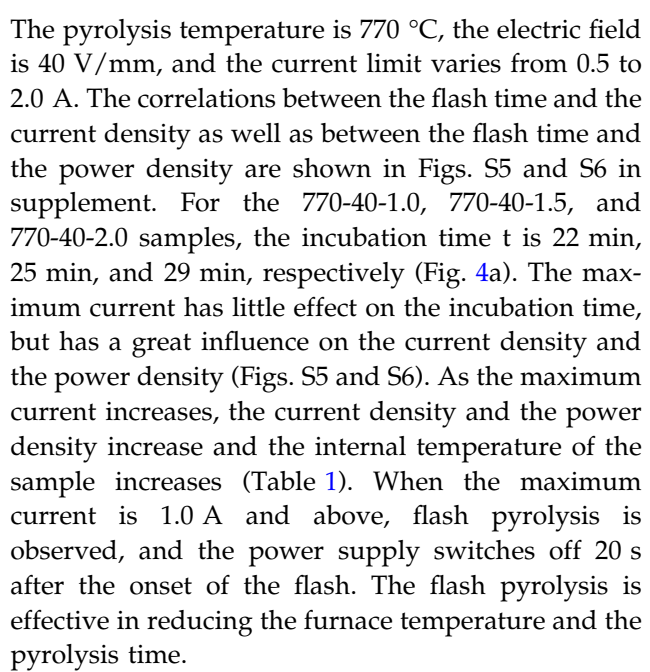


Figure 3 a Correlations between the flash time and the applied electric field, and b XRD patterns at different electric field.

doubles that of the higher electrical field conditions, at ~ 55 min, due to the lowest internal temperature of 1261.2 °C and the lowest electrical field. The reason is that the flash incubation time is related to the ordering of C, which depends on C diffusion. A lower electric field means slower C diffusion, which lengthens the incubation time. From Eq. (3), for the 770-30-2.0, 770-40-2.0, and 770-50-2.0 samples, the SiC crystallite sizes are 7.3 nm, 7.8 nm, and 7.5 nm, respectively (Fig. 4c), consistent with the results in Fig. 3b.

Effect of maximum current

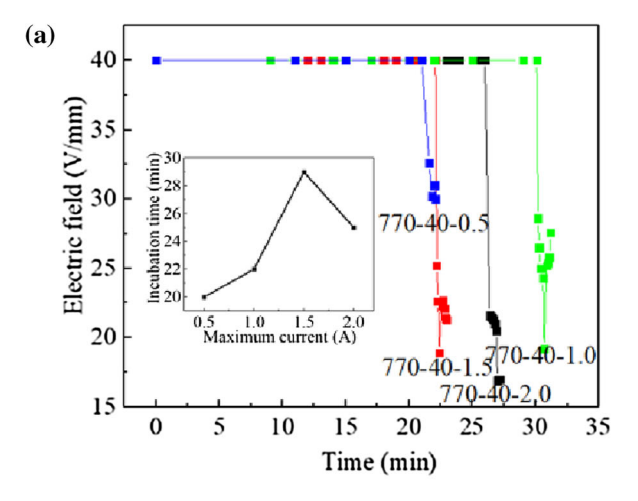
The effect of the current limit during the flash pyrolysis has also been studied. The corresponding electric field change versus time and the XRD patterns are provided in Figs. 3b and 4a, respectively.

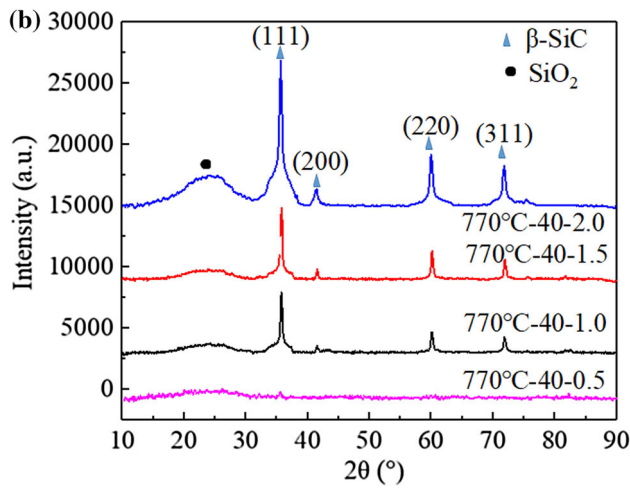


As the maximum current increases, the Joule heating increases and the applied electric field causes the crystallization of SiC. Figure 4b shows the XRD patterns of the samples at different maximum current. For the sample under 0.5 A current limit, only weak β-SiC diffraction peaks are seen. As shown in Table 1, the low current density of 0.5 A can only heat the sample to ~ 1127.5 °C through the Joule heating and cannot cause extensive SiC formation compared to the ~ 1345.2 °C internal temperature for the 770-40-2.0 sample. Thus, the XRD patterns show an amorphous SiO_2 phase ($\sim 22^\circ$) and a weak crystalline β-SiC phase (JCPDS Card No. 01-073-1665). From Eq. (3), for the 770-40-1.0, 770-40-1.5, and 770-40-2.0 samples, the SiC crystallite sizes are 7.3 nm, 7.8 nm, and 7.8 nm, respectively (Fig. 4c), again consistent with the results in Figs. 2b and 3b.

The TEM images for the samples pyrolyzed without any electric field and with different electric field at 770 °C are given in Fig. 5. After 770 °C pyrolysis without any electric field (Fig. 5a), the carbon phase is totally amorphous and shows no texture. For the 770-40-1.0 sample (Fig. 5b), at 40 V/mm electric field and 1.0 A current limit, the carbon phase remains amorphous even though 2–3 carbon layers start to line up. As the current increases, the Joule heating increases and the applied electric field causes the formation of the crystalline SiC phase. This means that the electrical field dictates the SiC atomic level arrangement, consistent with the SiC peaks in Fig. 4b. However, when the current limit increases to 2 A







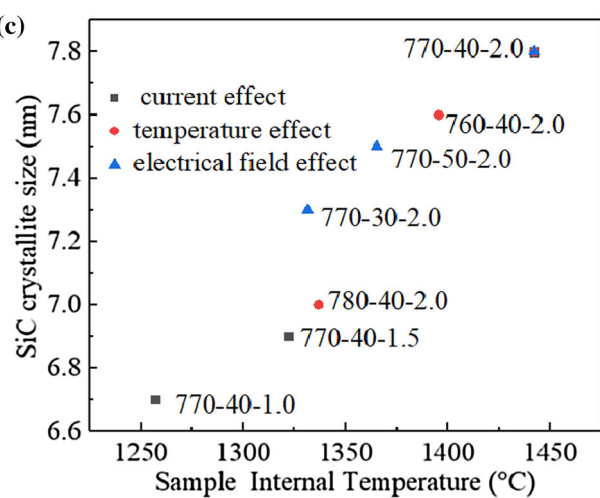


Figure 4 a Relationships between the incubation time for flash and the applied electric field, b XRD patterns at different maximum current, and c relation between the SiC crystallite size calculated from Eq. (3) and the internal temperature.

(Fig. 5c), local carbon ordering happens throughout the sample with 3–4 graphene layers arranged into a

crystalline structure. Under a high power density, significant Joule heating is induced, the 770-40-2.0 sample has much larger sizes and more ordered carbon regions. In addition, the β-SiC crystalline phase further develops. Although the length of the ordered carbon is about 10 nm, due to the small number of the graphene layers (2-4), there is no strong XRD peak in Fig. 4b. The nanocrystalline β-SiC is < 8 nm in size and localized as islands in the amorphous SiOC matrix. The SiOC specimen pyrolyzed at 1400 °C without any electric field demonstrates that the SiOC matrix phase contains areas of turbostratic carbon (~ 4 nm) and nanocrystalline β -SiC clusters of ~ 3.5 nm (Fig. 5d). The SiC crystallite sizes of the 770-40-2.0 and 1400-0-0.0 samples are only slightly greater than those calculated from Eq. (3), consistent with the XRD results in Fig. 4c. This again confirms that under the applied electric field, the carbon ordering and SiC crystallization increase.

Ceramic yield and thermal stability

Figure 6 shows the ceramic yields of the samples. Flash pyrolysis has a tremendous impact on the ceramic yield when compared to the 1400 °C pyrolyzed sample without any electrical field (the ceramic yield is 78.64%, as shown by the ★ symbol). As the pyrolysis temperature increases, the ceramic yield decreases. For the 760-40-2.0, 770-40-2.0, and 780-40-2.0 samples, the ceramic yield is 72.71, 53.37, and 44.18%, respectively, the percent decrease is 7.54, 32.15, and 43.82%, respectively. As the maximum current increases, the ceramic yield also decreases. For the 770-40-0.5, 770-40-1.0, 770-40-1.5, and 770-40-2.0 samples, the ceramic yield is 57.44, 53.53, 51.43, and 53.37%, respectively, the percent decrease is 26.96, 31.90, 34.60, and 32.15%, respectively. In addition, the ceramic yield decreases significantly with the electric field increase, from 78.64% for the 1400 °C without any electric field condition to 55.60% at 20 V/mm, 54.32% at 30 V/mm, 53.37% at 40 V/ mm, and 48.14% at 50 V/mm. The percent decrease is 29.30, 30.93, 32.15, and 38.78%, respectively. Overall, the temperature effect is largest and the current effect is smallest. The drastic ceramic yield decrease is a result of rapid loss of carbon radicals under the electrical field. Higher pyrolysis temperature and higher electrical field impose higher phase evolution driving forces and thus more weight loss.



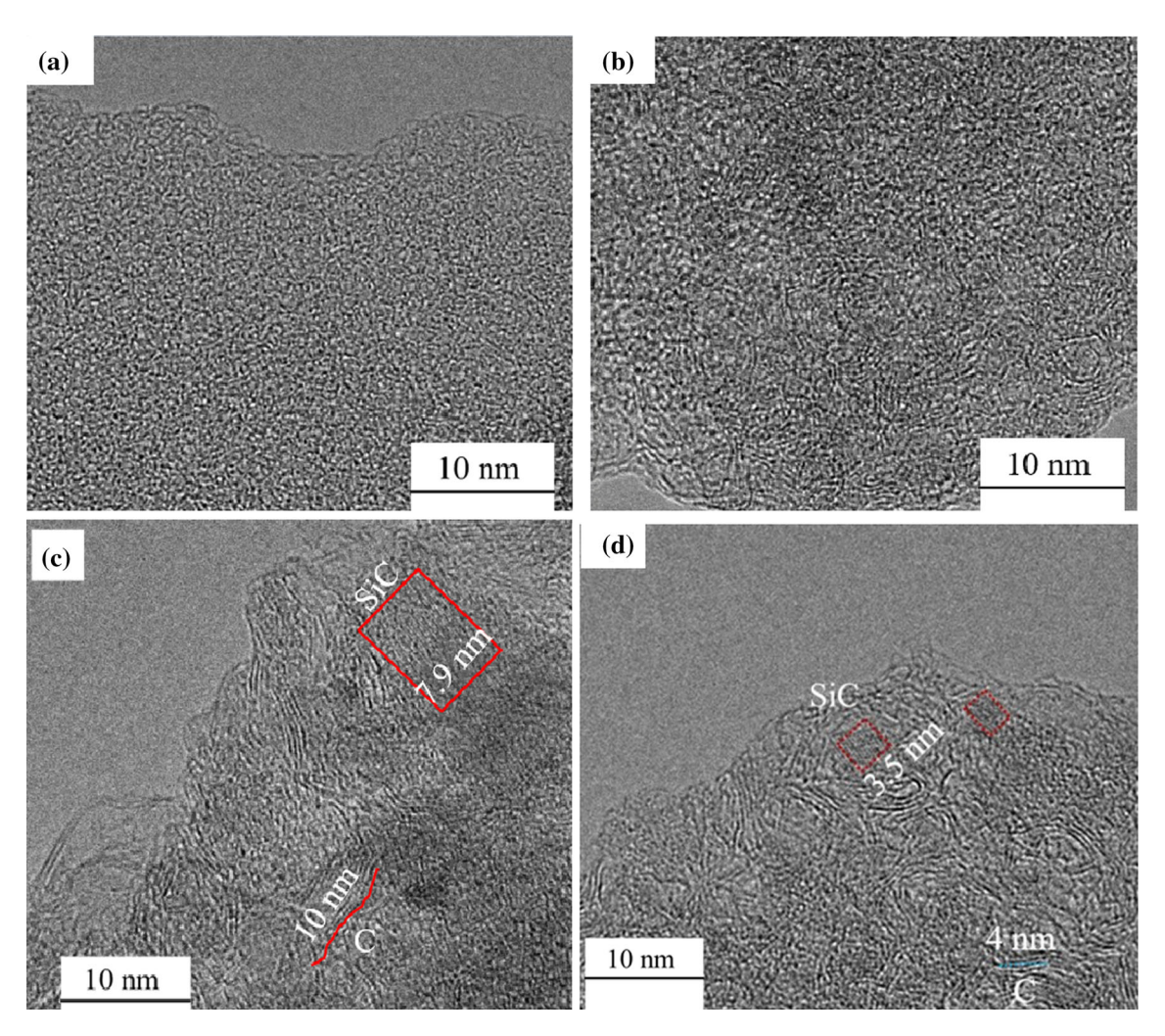


Figure 5 TEM microstructures of the samples: a 770-0-0, b 770-40-1.0, c 770-40-2.0, and d 1400 °C pyrolysis sample with no electric field.

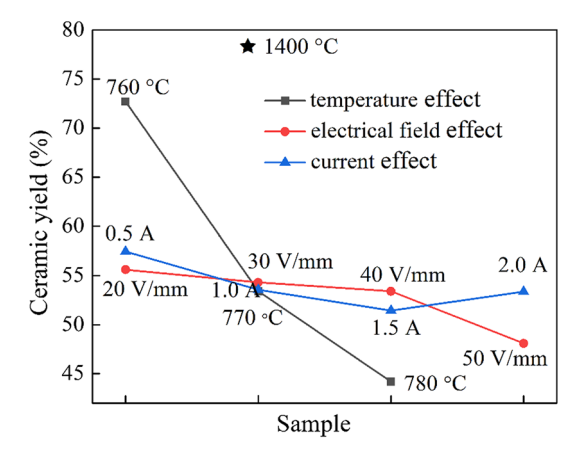
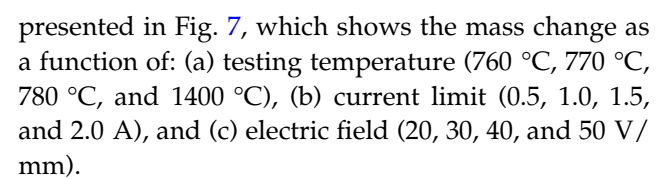


Figure 6 Ceramic yield of the SiOC samples.

In this study, the major focus on the thermal stability is for air atmosphere, which is oxidative and of most concern. The obtained TGA curves are



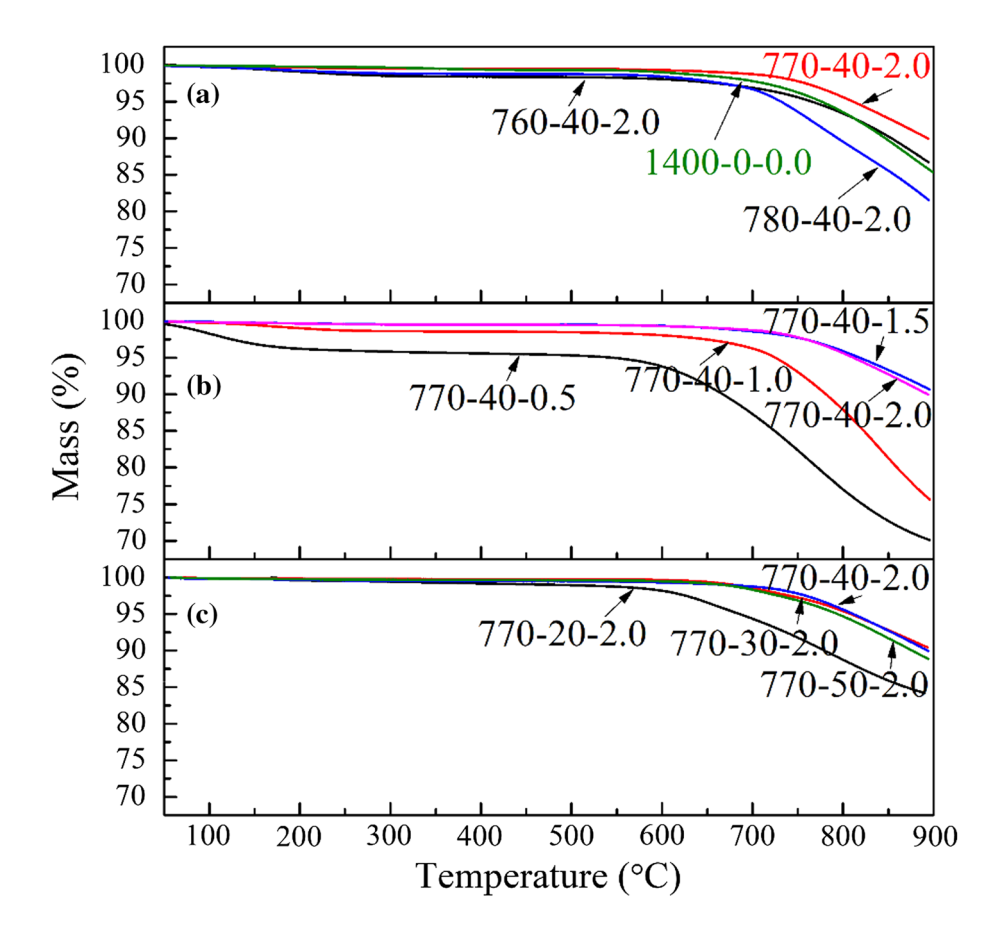
Based on the SiOC compositions, there are three unstable sources: free C, SiOC clusters, and SiC. For the free C, tiny graphene layers with edge C atoms can be oxidized; the radical species on the surface of free C can also be easily oxidized [28]. In the 400–800 °C range, the specific oxidation mechanism is the combustion of the free C phase [29].

$$C(\text{free}) + O_2(g) \rightarrow CO_x(g) \uparrow$$
 (6)

At greater than 800 °C, it can be represented as:



Figure 7 TGA curves at different conditions: (a) testing temperature (760 °C, 770 °C, 780 °C, and 1400 °C), (b) current limit (0.5, 1.0, 1.5, and 2.0 A), and (c) electric field (20, 30, 40, and 50 V/mm).



$$SiOC(s) + O_2(g) \rightarrow SiO_2(s) + CO_x(g) \uparrow$$
 (7)

Equation (6) leads to weight loss. Equation (7) causes the SiOC units to become more vulnerable to oxidation although it could lead to weight gain. In Fig. 7, the SiOC samples show weight loss, meaning that mostly free C is oxidized according to Eq. (6).

Figure 7a shows that at the same electric field of 40 V/mm and maximum current of 2.0 A, the 760-40-2.0 and 780-40-2.0 samples are stable up to 640 °C before a gradual weight loss up to 13.3 wt% and 18.4 wt%, respectively, at 900 °C. The main weight loss occurs above 700 °C. For the 770-40-2.0 sample, however, the sample is stable up to 742 °C before a drastic weight loss of 10.0 wt% at 900 °C. Compared with the 1400 °C pyrolyzed control sample (stable up to 682 °C, with a total weight loss of 14.7% at 900 °C), the thermal stability of the 770-40-2.0 sample increases by 60 °C. The 770-40-2.0 sample has the highest thermal stability because of the phase separation and the carbon ordering induced by the electric field, ordered carbon is less likely to be oxidized than amorphous carbon following Eq. (6). In addition, the

electronic current offers the Joule heating to facilitate the SiC formation. Eventually, more free C is consumed in the 770-40-2.0 sample, which reduces the instability from carbon oxidation. The internal temperature of the 760-40-2.0 and 780-40-2.0 samples is lower than that of the 770-40-2.0 sample, and there is a large amount of free C, which leads to the decrease in thermal stability.

Figure 7b shows the TGA curves at different maximum current for the sample pyrolyzed at 770 °C and 40 V/mm. The 1.5 A and 2.0 A samples are stable up to 740 °C, at which a weight loss of \sim 2.0 wt% is measured. The 0.5 A and 1.0 A samples, however, are only stable up to 610 °C before a gradual weight loss up to 24.3 wt% and 29.7 wt%, respectively. This means that the maximum current has a significant effect on the thermal stability. As the maximum current increases, the power density increases, the internal temperature of the sample increases, and the carbothermal reduction of SiO₂ takes place by consuming the free C phase (Eq. 5). Because the 1.5 A and 2.0 A samples produce more SiC, the thermal stability is higher.



At different electrical field with the same pyrolysis temperature of 770 °C and maximum current of 2.0 A (Fig. 7c), the 30 V/mm, 40 V/mm, and 50 V/mm samples have the highest stability, up to 742 °C. The 770-20-2.0 sample is stable up to 605 °C before a gradual weight loss up to 16.8 wt%. The 770-20-2.0 sample has the lowest thermal stability because a lower electrical field has a smaller phase evolution driving force; it creates a more vulnerable system for thermal degradation due to the oxidation of SiOC (Eq. 7) [6].

Based on the thermal stability results in Fig. 7, the SiOC materials are relatively stable up to 742 °C in air. The higher thermal stability for the 770-30-2.0, 770-40-1.5, 770-40-2.0, and 770-50-2.0 samples is a result of the rapid loss of carbon radicals under the electrical field. Consistent with the ceramic yield results in Fig. 6, the 770-40-0.5 and 770-20-2.0 samples have lower thermal stability due to a lack of phase development and microstructure change.

Nucleation under electrical field

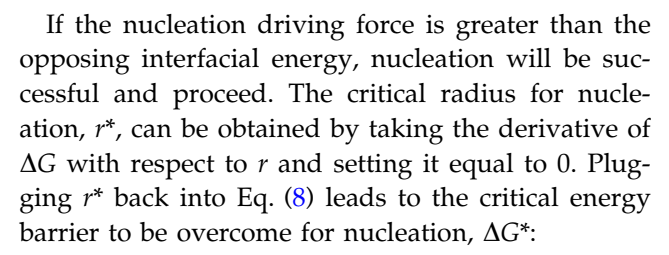
For the SiOC system, based on the classic nucleation theory, the nucleation driving force is from the total free energy decrease due to the formation of new phase embryos and is given by:

$$\Delta G = -\frac{4}{3}\pi r^3 \Delta G_{\rm V} + 4\pi r_{\rm E}^2 \tag{8}$$

where $\Delta G_{\rm V}$ is the polarization energy of SiC per unit volume and is given by Eq. (9) [30]. r is the nucleus radius. The growth of a nucleus is counteracted by the interfacial energy $\gamma_{\rm E}$ that the new species forms with the matrix lattice.

$$\Delta G_{\rm V} = \frac{1}{2} \varepsilon_{\rm o} \varepsilon_{\rm E} E^2 + \Delta G_{\rm V0} \tag{9}$$

where $\varepsilon_{\rm o}$ is the permittivity of free space at $8.85\times 10^{-12}~{\rm A}^2~{\rm s}^4/({\rm kg~m}),~\varepsilon_{\rm E}$ is the dielectric constant of the SiC nuclei and estimated to be 9.72 [31], and $\Delta G_{\rm V0}$ is the energy of formation per unit volume without an electric field, J/m³. $\Delta G_{\rm V0}$ can be converted from molar enthalpy [32] by multiplying by the density of SiC ($\sim 3.21\times 10^3~{\rm kg/m}^3$) [33, 34] and then dividing by the molar mass (40.11 \times 10⁻³ -kg/mol). The molar enthalpy $\Delta G_{\rm f}$ of β -SiC can be calculated by the Thermocalc® software as given in Table S1 for different temperatures [35]. $\gamma_{\rm E}$ is estimated as 2 J/m² [36].



$$r^* = \frac{4\gamma_{\rm E}}{\varepsilon_0 \varepsilon_{\rm E} E^2 + 2\Delta G_{\rm V0}} \tag{10}$$

$$\Delta G^* = \frac{64\pi\gamma_{\rm E}^3}{3\left[\varepsilon_0\varepsilon_{\rm E}E^2 + 2\Delta G_{\rm V0}\right]^2} \tag{11}$$

The critical radius r^* (Eq. 10) and the critical energy barrier ΔG^* (Eq. 11) for all the samples are shown in Table S1. These values are almost the same regardless of the applied electric field because the nucleation driving force contribution from the electric field, $\varepsilon_0\varepsilon_E E_j^2$ in Eqs. (8–11), is 10 orders of magnitude smaller than the ΔG_{V0} term. Thus, ΔG_{V0} is the dominant factor impacting the critical nuclei size and the critical energy barrier than the $\varepsilon_0\varepsilon_E E_j^2$ term. Because of this, the resulting SiC nuclei sizes in both cases are similar.

For the turbostratic carbon, from the literature, the value of enthalpy of formation is $\sim 1.7 \times 10^9$ J/m³ [32], $\varepsilon_{\rm E}$ is ~ 10 [37], and $\gamma_{\rm E}$ is ~ 1 J/m² [30]. Based on Eqs. (10) and (11), the critical radius and the critical energy barrier are 1.2 nm and 5.6×10^{-18} J, respectively. The critical radius of carbon is higher than that of SiC. This is mainly caused by the different volume formation energy $\Delta G_{\rm V0}$ for C and SiC.

The concentration of stable SiC or C nuclei in the evolving SiOC matrix, N, is a function of ΔG^* and can be expressed as [30, 38]:

$$N = \exp\left(-\frac{\Delta G^*}{kT}\right) \tag{12}$$

where *k* is Boltzmann constant, 1.38×10^{-23} J/K, and *T* is the sample temperature.

From Eq. (12), the change of the nuclei concentration ratio $N_{\rm T}/N_0$ versus the sample internal temperature under different electric field, or at the same electric field under different current limit or pyrolysis temperature is given in Fig. 8. $N_{\rm T}$ is the nuclei concentration at a specific flash pyrolysis condition as indicated in Fig. 8. N_0 is the nuclei concentration at 770 °C without any electric field. When the furnace temperature is greater than 760 °C, the nucleation rate in the SiOC samples increases exponentially for



SiC and C. The nuclei concentrations are as high as $\sim 10^{43}$ and 10^{65} times, respectively, that without an electric field for the 770-40-2.0 sample. This is because the drastic temperature increase from the Ioule heating, followed by the sudden increase in the electrical conductivity, increases the rates of Si and C diffusion. When the power density is 320 mW mm³, the specimen temperature can be as high as 1345.2 °C, which is high enough to induce the phase separation of the 770-40-2.0 sample in just a few seconds. Thus, even though the critical nuclei size and the critical energy barrier do not change drastically under the flash electric field, the phase separation occurs and the crystallite concentrations are dramatically increased due to the Joule heating during the flash pyrolysis, causing much more SiC and C formation within the samples. These stable crystallites can also grow in the short duration of the flash to 6-8 nm size (Fig. 4c). This calculation is consistent with the observations from the XRD (Figs. 2b, 3b, 4b) and TEM (Fig. 5c) results.

Carbon ordering

A distinct characteristic for the flash pyrolysis is the onset of a rapid temperature increase along with a highly nonlinear increase in the sample conductivity. Since C is the only conductive phase in the SiOCs, the state of carbon in different samples should be examined.

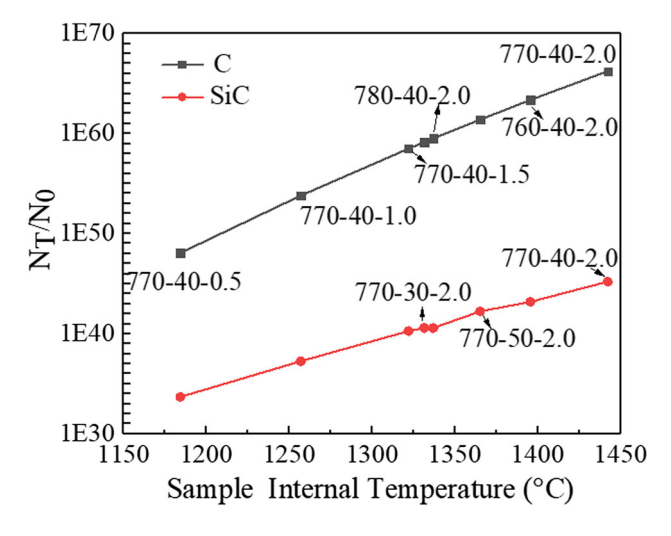


Figure 8 Effect of Joule heating on the stable nuclei concentration relative to the nuclei concentration at 770 °C under different electric field, or at the same electric field under different current limit or pyrolysis temperature.

Figure 9a shows the Raman spectra of the SiOC samples. The D_1 band at $\sim 1350 \text{ cm}^{-1}$ is ascribed to the defects and disordering in the free C, whereas the G band (in-plane vibrational mode) at 1588 cm⁻¹ is attributed to the ordered graphitic structure [39]. The broad G' band at 2682 cm⁻¹ and the weak band at 2934 cm⁻¹ can be assigned to a combination of the defective/disordering and graphitic mode (G + D), which are observed for the 770-40-1.0, 770-40-2.0, and 1400-0-0.0 samples.

Besides the well-studied D_1 and G peaks, the peak at $\sim 1500 \text{ cm}^{-1}$ belongs to amorphous carbon (D_3) [40, 41]. After the D_1 , G, and D_3 peaks are deconvoluted (Fig. 9a insert), their relative intensities $I(D_1)$, I(G), and $I(D_3)$ can be integrated. The results are provided in Table S2.

For the 740-0-0, 770-0-0, and 770-40-0.5 samples, there are only weak D_1 and G peaks, indicating that

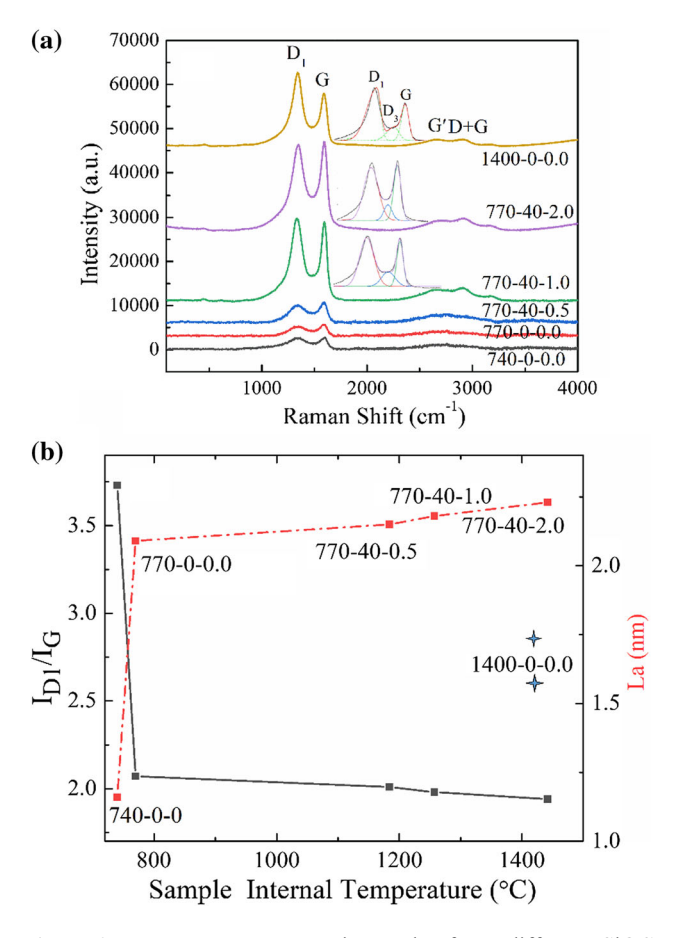


Figure 9 a Raman spectroscopic results from different SiOC samples. The inserts are deconvolution examples for the D_1 , G, and D_3 (amorphous C) peaks from the 770-40-1.0, 770-40-2, and 1400-0-0 samples. **b** Relationships between the I_D/I_G , L_a , and sample internal temperature.



the carbon is in an amorphous state. As the current limit (and thus power density) increases, the relative integrated intensity of the D_1 peak decreases, while that of the G peak increases, and the intensity ratio $I(D_1)/I(G)$ decreases (Fig. 9b). For the 770 °C-40-1.0 and 770 °C-40-2.0 samples, the D_3 peak decreases, while the G peak increases with the electric field; this change means that the samples experience an ordering from amorphous carbon into nanocrystalline carbon [40]. The increased carbon ordering is also observed for the 1400 °C-0-0.0 sample, showing a lower $I(D_3)$ and a higher I(G) compared to the 770 °C-0-0.0 sample. Regardless, the 1400 °C-0-0.0 sample still has a higher $I(D_3)$ peak and a lower I(G) peak compared to the 770 °C-40-1.0 and 770 °C-40-2.0 specimens. This means that the flash pyrolysis can cause more drastic carbon phase ordering compared simply increasing the sample pyrolysis temperature.

Among all the models for carbon domain size estimation [41–44], we believe that the Tunistra and Koening relation [44] can best assess the carbon crystallite size L_a :

$$L_{\rm a} = C(\lambda L) \left(\frac{I_{\rm D1}}{I_{\rm G}}\right)^{-1} \tag{13}$$

where $C(\lambda_L)$ is the scaling coefficient and I_D/I_G is the ratio of the integral intensities of the D_1 and G bands. To assess $C(\lambda_L)$ for the employed excitation line λ = 514.5 nm, we use the approximation C (λ_L) \approx $C_0 + \lambda_L C_1$, where C_0 and C_1 are estimated to be - 12.6 nm and 0.033, respectively [41]. For a 514.5 nm laser, the coefficient is 4.362. The results based on Eq. (13) are given in Fig. 9b for the studied samples. At 740 °C, L_a increases from ~ 1.16 nm for the sample without an electric field to ~ 2.23 nm for the 770-40-2.0 sample. The 1400-0-0.0 sample only has a L_a value of ~ 1.60 nm, and the 770-40-0.5 and 770-40-1.0 samples have L_a values of 2.15 nm and 2.18 nm, respectively. These L_a values are slightly smaller than those observed by TEM (Fig. 5). The reason is that the HRTEM method determines the graphene layer thickness, while the XRD and Raman values determine the carbon nanocrystallite sizes [45]. Since the carbon layer is tortuous, the Raman spectroscopy can only provide the average size of the carbon nanocrystallites, so the La values from the Raman spectroscopy is smaller. Regardless, the applied electric field can activate and accelerate the carbon phase ordering at 640 °C lower temperature.

Carbon ordering driven by an electric field has been demonstrated for various carbonaceous materials [21, 46, 47]. Under the electric field, electromigration causes the transfer of momentum from drifting electrons to defects within the carbon phase, which is believed to be the main mechanism for carbon to reorganize. The momentum transfer increases defect mobility, causes them to diffuse out of the carbon phase, and leads to a more ordered carbon phase [21]. These processes are further accelerated by the accompanied Joule heating for the SiOC systems. The flux *J* for the defects under this momentum transfer is [21, 48, 49]:

$$J = N_{\rm o} D_{\rm o} Z * \left(\frac{eE}{kT}\right) \exp\left(\frac{-E_{\rm f,v}}{kT}\right) \exp\left(\frac{-E_{\rm a}}{kT}\right) \tag{14}$$

where $N_{\rm o}$ is the number of atomic sites per volume, $D_{\rm o}$ is a temperature independent diffusion preexponential, Z^* is the effective valence of the species under consideration, e is the elemental charge, 1.6×10^{-19} C, $E_{\rm f,v}$ is the formation energy of vacancies, 1.2×10^{-18} J [50, 51], and $E_{\rm a}$ is the activation energy for vacancy diffusion, 1.9×10^{-19} J [49, 50]. Equation (14) can be simplified as:

$$J = C \cdot J(E, T) \tag{15}$$

where C represents $N_{\rm o}D_{\rm o}Z^*$ (all material properties independent of the external field). J (E, T) represents $\left(\frac{eE}{kT}\right)\exp\left(\frac{-E_{\rm f,v}}{kT}\right)\exp\left(\frac{-E_{\rm a}}{kT}\right)$, which includes all the terms affected by the external electric field and the sample temperature. Figure 10 shows J (E, T) as a function of the sample internal temperature under different electric field.

The defect flux is 0 for the 770-0-0.0 sample because of a lack of significant Joule heating. The defect flux for the 770-40-0.5 and 770-50-2.0 samples are 2.5×10^{-25} m⁻¹ and 1.7×10^{-23} m⁻¹, respectively. Because of the smaller Joule heating, these J (E, T) values are significantly less than that for the 770-40-2.0 sample (4.0×10^{-21} m⁻¹). The increased sample internal temperature due to the Joule heating influences the defect flux more significantly. Subsequently, the graphitization is more affected by the Joule heating than the electric field. Thus, the driving force for the graphitization within the SiOC is the synergistic effect from both the Joule heating and the electromigration. If the sample internal temperature is low and the Joule heating is insignificant, the



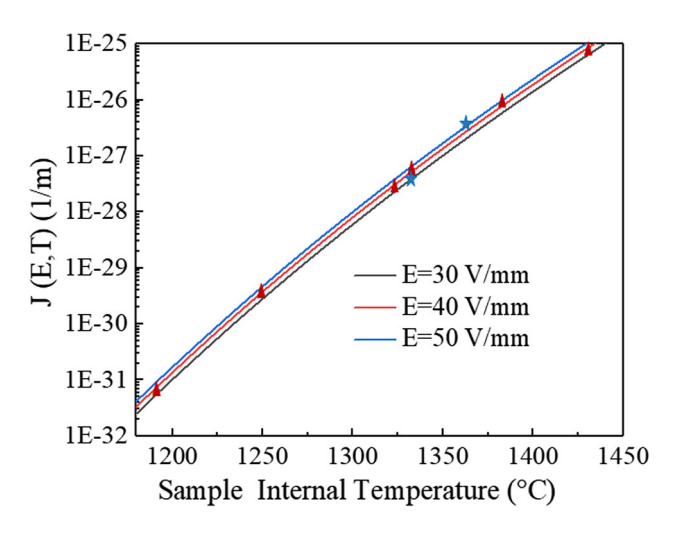


Figure 10 Correlation of J(E,T) with the sample internal temperature at different applied electric field. The star and traingle symbols represent the experimental conditions.

carbon phase cannot reorganize into a more ordered state from its original amorphous phase.

Fundamental process

With higher electric field, pyrolysis temperature, and current density, the SiOC samples show more mass loss, accompanied by more extensive formation of SiC and ordered carbon phases. The mechanisms of flash pyrolysis can be further explained as follows (Fig. 11). The phase separation during the flash pyrolysis has the characteristics of nucleation and growth [30]. During the incubation period, the electric field acts as an external driving force for the ordered carbon phase nucleation and then the SiC nuclei formation (Eqs. 8-12). The nucleation undergoes an incubation period that can increase from a few seconds to several thousand seconds with the applied electrical field decrease. As a result, more carbon forms with an increasing electric field. During the new phase growth period, the ordering of carbon is mainly through electromigration accompanied by a highly nonlinear increase in the conductivity of the specimen. The carbon ordering leads to an abrupt transition of the specimen from insulating to conducting. In this short, transient process, the Joule heating (Eq. 2) simultaneously increases the sample temperature and leads to further C and SiC formation through the SiOC phase separation (Eq. 4) or carbothermal reduction of SiO_2 (Eq. 5).

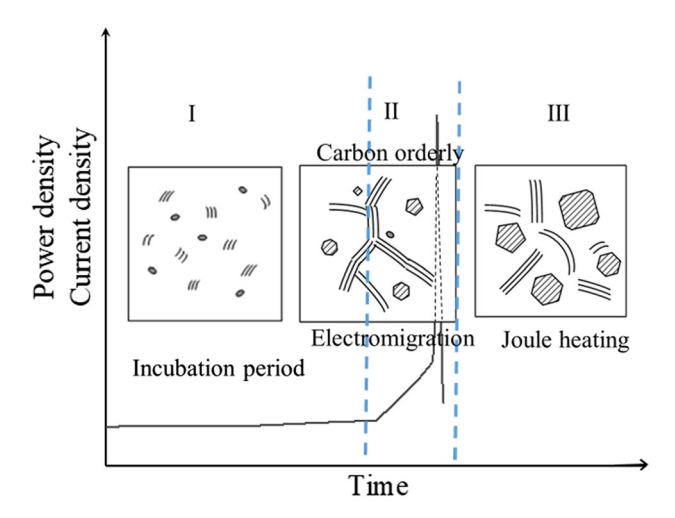


Figure 11 Schematic diagram illustrating the flash pyrolysis.

Conclusions

Flash pyrolysis has been successfully used to produce SiOC with accelerated phase evolution. At > 20 V/mm electric field, > 740 °C pyrolysis temperature, and > 0.5 A maximum limiting current, flash pyrolysis takes place and leads to more SiC formation and a more ordered carbon phase. The driving force for the accelerated SiOC phase evolution is a result of the applied electrical field. As the pyrolysis temperature, the electric field, and the maximum current increase, the ceramic yield decreases. The resulting SiOC samples are stable up to 742 °C in air. From the mechanistic point of view, the applied electric field induces simultaneous Joule heating and electromigration. These two factors in combination cause carbon ordering and SiC formation. Flash pyrolysis can be used as a new efficient process for making polymer-derived SiOC materials.

Acknowledgements

We acknowledge the financial support from National Science Foundation under grant number CMMI-1634325.

Electronic supplementary material: The online version of this article (https://doi.org/10.1007/s108 53-019-03315-z) contains supplementary material, which is available to authorized users.



References

- [1] Li J, Lu K (2015) Highly porous SiOC bulk ceramics with water vapor assisted pyrolysis. J Am Ceram Soc 98(8):2357–2365
- [2] Soraru GD, Dallapiccola E, Andrea GD (1996) mechanical characterization of sol–gel-derived silicon oxycarbide glasses. J Am Ceram Soc 79(8):2074–2080
- [3] Esfehanian M, Oberacker R, Fett T, Hoffmann MJ (2008) Development of dense filler-free polymer-derived SiOC ceramics by field-assisted sintering. J Am Ceram Soc 91(11):3803–3805
- [4] Clark MD, Walker LS, Hadjiev VG, Khabashesku V, Corral EL, Krishnamoorti R (2011) Fast sol–gel preparation of silicon carbide–silicon oxycarbide nanocomposites. J Am Ceram Soc 94(12):4444–4452
- [5] Du B, Hong CQ, Zhang XH, Wang JZ, Qu Q (2018) Preparation and mechanical behaviors of SiOC-modified carbon-bonded carbon fiber composite with in situ growth of three-dimensional SiC nanowires. J Eur Ceram Soc 38(5):2272–2278
- [6] Lu K, Erb D, Liu MY (2016) Thermal stability and electrical conductivity of carbon-enriched silicon oxycarbide. J Mater Chem C 4(9):1829–1837
- [7] Colombo P, Mera G, Riedel R, Soraru GD (2010) Polymerderived ceramics: 40 years of research and innovation in advanced ceramics. J Am Ceram Soc 93(7):1805–1837
- [8] Zhu SM, Ding SQ, Xi HA, Wang RD (2005) Low-temperature fabrication of porous SiC ceramics by preceramic polymer reaction bonding. Mater Lett 59(5):595–597
- [9] Kawamura F, Yamane H, Yamada T, Yin S, Sato T (2008) Low-temperature fabrication of porous beta-SiC ceramics in sodium vapor. J Am Ceram Soc 91(1):51–55
- [10] Kim KJ, Lee S, Lee JH, Roh MH, Lim KY, Kim YW (2009) Structural and optical characteristics of crystalline silicon carbide nanoparticles synthesized by carbothermal reduction. J Am Ceram Soc 92(2):424–428
- [11] Yang K, Yang Y, Lin ZM, Li JT, Du JS (2007) Mechanical-activation-assisted combustion synthesis of SiC powders with polytetrafluoroethylene as promoter. Mater Res Bull 42(9):1625–1632
- [12] Brequel H, Parmentier J, Soraru GD, Schiffini L, Enzo S (1999) Study of the phase separation in amorphous silicon oxycarbide glasses under heat treatment. Nanostruct Mater 11(6):721–731
- [13] Saha A, Raj R (2007) Crystallization maps for SiCO amorphous ceramics. J Am Ceram Soc 90(2):578–583
- [14] Saha A, Raj R, Williamson DL (2006) A model for the nanodomains in polymer-derived SiCO. J Am Ceram Soc 89(7):2188–2195

- [15] Brequel H, Parmentier J, Walter S, Badheka R, Trimmel G, Masse S, Latournerie J, Dempsey P, Turquat C, Desmartin-Chomel A, Le Neindre-Prum L, Jayasooriya UA, Hourlier D, Kleebe HJ, Soraru GD, Enzo S, Babonneau F (2004) Systematic structural characterization of the high-temperature behavior of nearly stoichiometric silicon oxycarbide glasses. Chem Mater 16(13):2585–2598
- [16] Cologna M, Rashkova B, Raj R (2010) Flash sintering of nanograin zirconia in < 5 s at 850 °C. J Am Ceram Soc 93(11):3556–3559
- [17] Raj R (2012) Joule heating during flash-sintering. J Eur Ceram Soc 32(10):2293–2301
- [18] Grasso S, Sakka Y, Rendtorff N, Hu CF, Maizza G, Borodianska H, Vasylkiv O (2011) Modeling of the temperature distribution of flash sintered zirconia. J Ceram Soc Jpn 119(1386):144–146
- [19] Mazo MA, Palencia C, Nistal A, Rubio F, Rubio J, Oteo JL (2012) Dense bulk silicon oxycarbide glasses obtained by spark plasma sintering. J Eur Ceram Soc 32(12):3369–3378
- [20] Sujith R, Srinivasan N, Kumar R (2013) Small-scale deformation of pulsed electric current sintered silicon oxycarbide polymer derived ceramics. Adv Eng Mater 15(11):1040–1045
- [21] Wang B, Wolfe DE, Terrones M, Haque MA, Ganguly S, Roy AK (2017) Electro-graphitization and exfoliation of graphene on carbon nanofibers. Carbon 117:201–207
- [22] Cologna M, Francis JSC, Raj R (2011) Field assisted and flash sintering of alumina and its relationship to conductivity and MgO-doping. J Eur Ceram Soc 31(15):2827–2837
- [23] Francis JSC, Raj R (2012) Flash-sinterforging of nanograin zirconia: field assisted sintering and superplasticity. J Am Ceram Soc 95(1):138–146
- [24] Yoshida H, Sakka Y, Yamamoto T, Lebrun JM, Raj R (2014) Densification behaviour and microstructural development in undoped yttria prepared by flash-sintering. J Eur Ceram Soc 34(4):991–1000
- [25] Torabi M, Sadrnezhaad SK (2011) Electrochemical evaluation of nanocrystalline Zn-doped tin oxides as anodes for lithium ion microbatteries. J Power Sources 196(1):399–404
- [26] Erb D, Lu K (2017) Additive and pyrolysis atmosphere effects on polysiloxane-derived Porous SiOC ceramics. J Eur Ceram Soc 37(15):4547–4557
- [27] Lu K (2015) Porous and high surface area silicon oxycarbide-based materials—a review. Mater Sci Eng R 97:23–49
- [28] Lu K, Erb D, Liu MY (2016) Phase transformation, oxidation stability, and electrical conductivity of TiO₂-polysilox-ane derived ceramics. J Mater Sci 51(22):10166–10177. https://doi.org/10.1007/s10853-016-0244-6
- [29] Brewer CM, Bujalski DR, Parent VE, Su K, Zank GA (1999) Insights into the oxidation chemistry of SiOC



- ceramics derived from silsesquioxanes. J Sol Gel Sci Technol 14(1):49-68
- [30] Naik KS, Sglavo VM, Raj R (2014) Flash sintering as a nucleation phenomenon and a model thereof. J Eur Ceram Soc 34(15):4063–4067
- [31] Kleykamp H (1998) Gibbs energy of formation of SiC: a contribution to the thermodynamic stability of the modifications. Ber Bunsen Phys Chem 102(9):1231–1234
- [32] Tavakoli AH, Armentrout MM, Narisawa M, Sen S, Navrotsky A (2015) White Si-O-C ceramic: structure and thermodynamic stability. J Am Ceram Soc 98(1):242-246
- [33] Pradere C, Batsale JC, Goyhénèche JM, Pailler R, Dilhaire S (2009) Thermal properties of carbon fibers at very high temperature. Carbon 47(3):737–743
- [34] Sazali NES, Deraman M, Omar R, Othman MAR, Suleman M, Shamsudin SA, Tajuddin NSM, Hanappi MFYM, Hamdan E, Nor NSM, Basri NH (2016) Preparation and structural characterization of turbostratic-carbon/graphene derived from amylose film. AIP Conf Proc 1784(1):040009
- [35] Kay DAR, Taylor J (1960) Activities of silica in the lime + alumina + silica system. Trans Faraday Soc 56(9):1372–1386
- [36] Minnear WP (1982) Interfacial energies in the Si/SiC system and the Si + C reaction. J Am Ceram Soc 65(1):C10–C11
- [37] Kim T, Lee J, Lee K-H (2016) Full graphitization of amorphous carbon by microwave heating. RSC Adv 6(29):24667–24674
- [38] Fisher JC, Hollomon JH, Turnbull D (1948) Nucleation. J Appl Phys 19(8):775–784
- [39] Pan JM, Pan JF, Cheng XN, Yan XH, Lu QB, Zhang CH (2014) Synthesis of hierarchical porous silicon oxycarbide ceramics from preceramic polymer and wood biomass composites. J Eur Ceram Soc 34(2):249–256
- [40] Roth F, Waleska P, Hess C, Ionescu E, Nicoloso N (2016) UV Raman spectroscopy of segregated carbon in silicon oxycarbides. J Ceram Soc Jpn 124(10):1042–1045

- [41] Larouche N, Stansfield BL (2010) Classifying nanostructured carbons using graphitic indices derived from Raman spectra. Carbon 48(3):620–629
- [42] Ferrari AC, Robertson J (2000) Interpretation of Raman spectra of disordered and amorphous carbon. Phys Rev B 61(20):14095–14107
- [43] Cuesta A, Dhamelincourt P, Laureyns J, Martinez-Alonso A, Tascon JMD (1998) Comparative performance of X-ray diffraction and raman microprobe techniques for the study of carbon materials. J Mater Chem 8(12):2875–2879
- [44] Tuinstra F, Koenig JL (1970) Raman spectrum of graphite. J Chem Phys 53(3):1126–1130
- [45] Zhang XF, Yan QG, Leng WQ, Li JH, Zhang JL, Cai ZY, Hassan E (2017) Carbon nanostructure of kraft lignin thermally treated at 500 to 1000 °C. Materials 10(8):975
- [46] Jia X, Hofmann M, Meunier V, Sumpter BG, Campos-Delgado J, Romo-Herrera JM, Son H, Hsieh Y-P, Reina A, Kong J, Terrones M, Dresselhaus MS (2009) Controlled formation of sharp zigzag and armchair edges in graphitic nanoribbons. Science 323(5922):1701–1705
- [47] Wang BM, Haque MA, Mag-isa AE, Kim JH, Lee HJ (2015) High temperature and current density induced degradation of multi-layer graphene. Appl Phys Lett 107(16):163103
- [48] Huang YF, Deng ZX, Wang WL, Liang CL, She JC, Deng SZ, Xu NS (2015) Field-induced crystalline-to-amorphous phase transformation on the Si nano-apex and the achieving of highly reliable si nano-cathodes. Sci Rep UK 5:10631
- [49] de Orio RL, Ceric H, Selberherr S (2010) Physically based models of electromigration: from black's equation to modern TCAD models. Microelectron Reliab 50(6):775–789
- [50] Wadey JD, Markevich A, Robertson A, Warner J, Kirkland A, Besley E (2016) Mechanisms of monovacancy diffusion in graphene. Chem Phys Lett 648:161–165
- [51] Tian WC, Li WH, Yu WB, Liu XH (2017) A review on lattice defects in graphene: types, generation, effects and regulation. Micromachines Basel 8(5):1–15

